Passive seismic reflection interferometry

A case study from the aquistore CO_2 storage site, Saskatchewan, Canada

Cheraghi, Saeid; White, Donald J.; Draganov, Deyan; Bellefleur, Gilles; Craven, James A.; Roberts, Brian

DOI
10.1190/GEO2016-0370.1

Publication date
2017

Document Version
Final published version

Published in
Geophysics

GEOPHYSICS, VOL. 82, NO. 3 (MAY-JUNE 2017); P. B79–B93, 13 FIGS., 6 TABLES.
10.1190/GEO2016-0370.1

Case History

Passive seismic reflection interferometry: A case study from the Aquistore CO_2 storage site, Saskatchewan, Canada

Saeid Cheraghi[1], Donald J. White[1], Deyan Draganov[2], Gilles Bellefleur[1], James A. Craven[1], and Brian Roberts[1]

ABSTRACT

Seismic reflection interferometry has recently been tested in a few resource-exploration applications. We have evaluated passive seismic interferometry results for data from the Aquistore CO_2 storage site, Saskatchewan, Canada, with the objective of testing the method's ability to image the subsurface geology and its potential for time-lapse imaging. We analyzed passive seismic data recorded along two perpendicular geophone lines for two time periods that include 23 days in June 2014 and 13 days in February 2015. Beam-forming analysis showed that a nearby power plant is the dominant source of ambient noise. We retrieved virtual shot gathers not only by correlating long noise panels (1 h) for both recording periods, but also by correlating shorter noise panels (10 s) from two days of each recording period. We applied illumination diagnosis to the noise panels from the two chosen days for each period to help suppress the surface waves. Comparisons of the common-midpoints stacked sections, resulting from the virtual shot gathers, with colocated active-source images and log-based synthetic seismograms showed that the best ambient-noise images were obtained for the longest recording periods. The application of illumination diagnosis revealed that only a small percentage of the noise panels are dominated by body waves. Thus, images formed using only this subset of noise panels failed to improve the images obtained from the 23 and 13 days of noise recording. To evaluate the passive images, we performed log-based correlations that showed moderate correlation ranging from approximately 0.5–0.65 in the two-way time range of 0.8–1.5 s. For the 13 to 23 days of noise used in our analysis, the resulting images at the reservoir depth of 3200 m or ~1.85 s are unlikely to be suitable for time-lapse imaging at this site. This is most likely due to the limited directional illumination and dominance of surface-wave noise.

INTRODUCTION

Active-source seismic reflection surveys have been widely used to monitor underground CO_2 storage (Eiken et al., 2011; Ivandic et al., 2012; Arts et al., 2013; White, 2013a, 2013b). Though effective, 3D time-lapse seismic monitoring is relatively expensive. Ambient-noise interferometry has the potential of providing a less expensive alternative technique, but it must first be successfully demonstrated that it can provide reliable monitoring results at a specific field site with a proposed geometry. Seismic interferometry has been tested with some success for seismic reflection imaging in mineral and oil exploration applications (Draganov et al., 2007, 2009, 2013; Nakata et al., 2011; Xu et al., 2012; Cheraghi et al., 2015), but to date, feasibility studies for CO_2 storage monitoring with passive seismic interferometry are limited (Xu et al., 2012; Boullenger et al., 2015; Gassenmeier et al., 2015).

In this study, we evaluate the use of passive seismic interferometry for reflection imaging at the Aquistore CO_2 storage site near Estevan, Saskatchewan, Canada (see Figure 1 for location). The main goals of this study are (1) to image the subsurface geology

Manuscript received by the Editor 14 July 2016; revised manuscript received 10 November 2016; published online 27 February 2017.
[1]Geological Survey of Canada, Ottawa, Ontario, Canada. E-mail: saeid.cheraghi@canada.ca; don.white@canada.ca; gilles.bellefleur@canada.ca; jim.craven@canada.ca; brian.roberts@canada.ca.
[2]Delft University of Technology, Department of Geoscience and Engineering, Delft, The Netherlands. E-mail: d.s.draganov@tudelft.nl.

in the vicinity of the storage reservoir at 3200 m depth and (2) to assess the potential for time-lapse imaging based on the consistency of images produced from two different recording periods. We show the results of passive seismic interferometry for data acquired with permanently deployed receivers along two orthogonal lines. Data from two time periods of the passive recording are analyzed: 23 days in June 2014 and 13 days in February 2015. Different approaches for retrieving virtual shot gathers are investigated including the use of different time-window lengths for the noise panels (one hour versus 10 s) and slowness criteria for choosing noise panels that might be dominated by body waves. The quality of the resultant images is assessed from their comparison with existing active-source 3D seismic data and well-based synthetic seismograms from the site. Finally, the challenges and prospects of using this method for the monitoring of this CO_2 site are discussed.

THE AQUISTORE CO_2 STORAGE SITE

The Aquistore CO_2 storage site (Worth et al., 2014) is located approximately 5 km southwest of the town of Estevan, Saskatchewan, Canada (Figure 1). This site affords a good opportunity for evaluation of seismic interferometry for reflection imaging as (1) the geology at this location is structurally simple consisting of subhorizontal layers (White et al., 2016), (2) a permanent array of buried geophones passively records data continuously at the site (White et al., 2015), and (3) an existing 3D active-source seismic data volume exists for direct comparison (Roach et al., 2015; White et al., 2016).

Two orthogonal lines (L1 and L2, Figure 1) of permanently buried geophones provide continuous recording of ambient noise at the Aquistore site. The primary purpose of these geophones is to provide continuous monitoring of injection-induced microseismicity. These geophones are a subset of a larger 2D grid of geophones that have been deployed for ongoing time-lapse seismic monitoring at the site (Roach et al., 2015; White et al., 2015). Details concerning the geophone arrays are provided in Table 1. Recording of ambient noise along lines L1 and L2 was started in July 2012.

The Aquistore site lies within the northern portion of the Williston Basin where approximately 3350 m of Paleozoic-to-Tertiary sedimentary rocks overlie crystalline Precambrian rocks. The sedimentary units dip gently to the south-southeast at approximately 1°–2°. The CO_2 storage reservoir includes the Deadwood and Winnipeg formations, which constitute a 200 m thick sequence of sandstones with interbeds of silt, shale, and carbonate that lie immediately above the Precambrian basement rocks. The uppermost unit of the Winnipeg Formation is a 15 m thick shale, which forms the caprock of the reservoir. The reservoir is the primary target of the seismic investigation, although the overlying units are also of interest with regard to monitoring for potential migration of CO_2 upward from the reservoir.

The Aquistore site is a relatively quiet area in terms of ambient noise. The major human activities occur near the town of Estevan and the Boundary Dam power plant located approximately 3 km east of the Aquistore site (Figure 1).

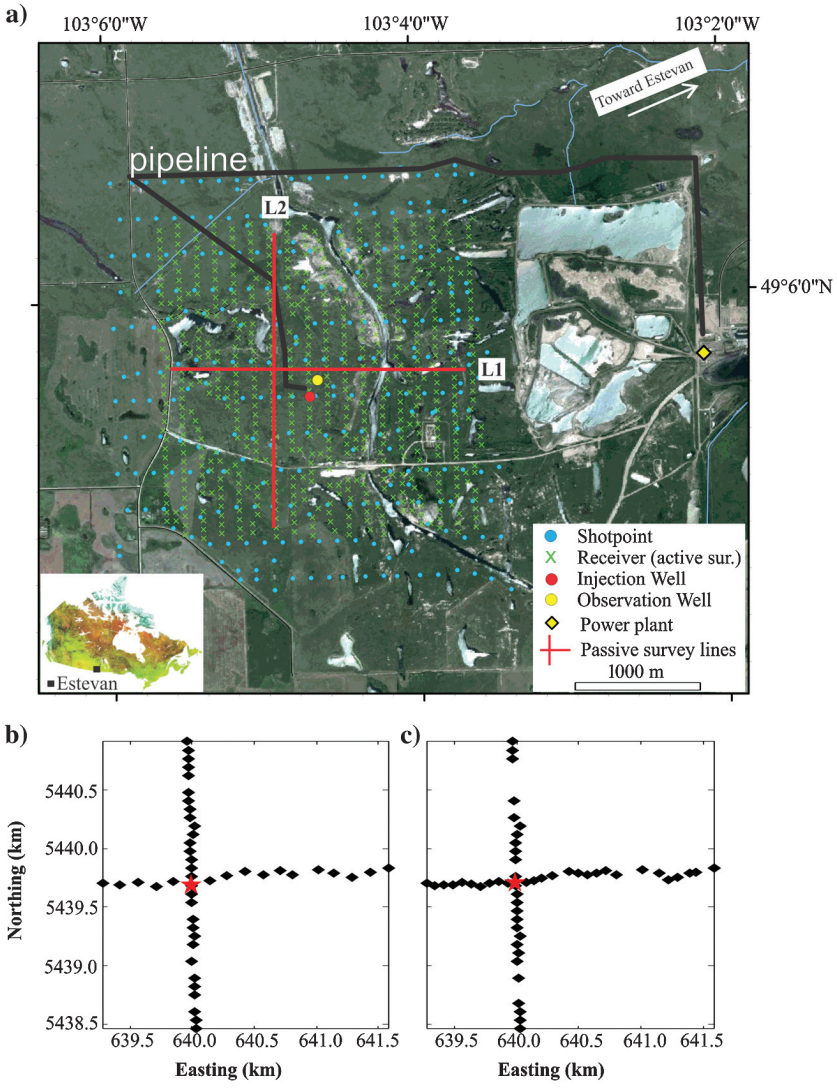

Figure 1. (a) Map of the Aquistore CO_2 injection site showing shotpoints (blue circles) and permanently deployed receivers (green crosses) of the 3D active-source seismic survey. Two passive survey lines (red lines), L1 and L2, are oriented west–east and south–north, respectively. The location of the power plant, CO_2 pipeline, injection, and observation wells are also shown. The town of Estevan is located 5 km northeast of the site. The inset shows a map of Canada and the Aquistore site location. Locations of the active receivers are shown, which recorded ambient noise during (b) June 2014 and (c) February 2015. The geometric attributes of both lines are shown in Table 1. The red star in panels (b and c) shows the receiver at the intersections of L1 and L2.

METHODOLOGY

We seek to retrieve virtual shot gathers from ambient noise recordings for the purpose of common-midpoints (CMP) reflection processing. Virtual shot gathers can be retrieved using the relation:

$$\{\mathbf{g}_{p,q}(\mathbf{x_A},\mathbf{x_B},t)+\mathbf{g}_{p,q}(\mathbf{x_A},\mathbf{x_B},-t)\} * \mathbf{s}(t) = \; <\mathbf{v}_p(\mathbf{x_A},-t) * \mathbf{v}_q(\mathbf{x_B},t)> \qquad (1)$$

(Wapenaar, 2004; Draganov et al., 2009). The terms $\mathbf{g}_{p,q}(\mathbf{x_A},\mathbf{x_B},t)$ and $\mathbf{g}_{p,q}(\mathbf{x_A},\mathbf{x_B},-t)$ in the left side of equation 1 represent Green's function (causal part) and its time-reversed version (acausal part) between two receiver positions $\mathbf{x_A}$ and $\mathbf{x_B}$. Green's functions are convolved with the average autocorrelation $\mathbf{s}(t)$ of the source time function of the noise sources. The terms on the right side represent the crosscorrelation of the particle velocity recorded in the p and q directions ($p,q=1,2,3$) at $\mathbf{x_A}$ and $\mathbf{x_B}$. The angle brackets imply the temporal summation over all correlated noise panels.

Ambient noise sources generally produce a variety of seismic-wave types including surface waves, refracted, and reflected body waves (Roux et al., 2005; Draganov et al., 2009; Zhang et al., 2009; Ruigrok et al., 2010; Poli et al., 2012; Behm et al., 2014; Jeong and Byun, 2014). Commonly, virtual shot gathers retrieved from ambient noise using equation 1 are dominated by surface waves whereas reflected or scattered body waves have relatively low amplitudes. This can be problematic when the goal is to perform seismic reflection imaging (Draganov et al., 2013). Various methods have been proposed to eliminate or reduce the effects of the surface waves in virtual shot gathers. Filtering of noise panels (Ruigrok et al., 2011) and beam-forming analysis (Draganov et al., 2013) are two methods that have been used. Standard multichannel CMP reflection processing of virtual shot gathers also helps enhance reflections and reduce surface-wave energy (Cheraghi et al., 2015).

An efficient method of surface-wave suppression during the retrieval of the virtual shot gathers was proposed by Almagro Vidal et al. (2014). The continuous ambient-noise recording is divided into shorter time windows. Each of these windows is correlated with its trace at the chosen virtual source position. This can be written as (Almagro Vidal et al., 2014)

$$\mathbf{c}^{\mathrm{i}}(\mathbf{x_B},\mathbf{x_A},t)=(\mathbf{u}^{\mathrm{obs}}(\mathbf{x_A},-t) * \mathbf{u}^{\mathrm{obs}}(\mathbf{x_B},t))_i, \qquad (2)$$

where $\mathbf{u}^{\mathrm{obs}}$ is the recorded ambient noise at $\mathbf{x_A}$ and $\mathbf{x_B}$, i is the number of the correlated noise panels, $*$ is the crosscorrelation operator, and $\mathbf{c}(\mathbf{x_B},\mathbf{x_A},t)$ is the correlated noise between A and B. Equation 2 represents a single correlated noise panel. To retrieve a virtual shot panel, the individual correlated noise panels should be summed. To suppress the retrieval of surface waves in the final retrieved common-shot panel, Almagro Vidal et al. (2014) propose evaluation of the individual correlated noise panels for the presence of body-wave noise. If in the correlated panel body waves are dominant, the correlated noise panel is kept for the summation, whereas it is discarded if the body waves are subordinate. The evaluation procedure of the correlated noise panels ($\mathbf{c}^i$) is performed in the τ-p domain. At $\tau=0$, a correlated noise panel is (Almagro Vidal et al., 2014)

$$\mathbf{c}^{i\sim}(\mathbf{x_A},p)\equiv\int \mathbf{c}^i[\mathbf{x_B},\mathbf{x_A},p.(\mathbf{x_B}-\mathbf{x_A})]\mathrm{d}x_B. \qquad (3)$$

To decide if a correlated noise panel is dominated by body waves, ray-parameter limits are chosen based on the expected body- and surface-wave velocities for the study area. Readers are referred to Almagro Vidal et al. (2014) for more details on the illumination-diagnosis procedure.

DATA ANALYSYS AND RESULTS

Ambient noise assessment

To evaluate the feasibility of passive seismic interferometry for time-lapse seismic imaging, first a qualitative assessment was made of a part of the ambient noise recorded at the Aquistore site. We carefully inspected the recorded noise from different time periods and selected 23 days of data from June 2014 and 13 days of data from February 2015. These time periods were chosen because all receivers along L1 and L2 were operational (see Table 1 for the available receivers on each line). The number of geophones along L1 increased between June 2014 and February 2015 as infill geophones were added to the line to achieve a spacing (72 m) equivalent to that along L2. The lengths of the receiver spreads along L1 (2302 m) and L2 (2447 m) were consistent in June 2014 and February 2015.

The effective retrieval of body waves with seismic interferometry requires the choice of the time-window length for analysis. As discussed by Almagro Vidal et al. (2014), longer time windows contain ambient noise from different noise sources whereas shorter time windows may lower the chance of inclusion of body-wave noise from several different sources within the same window. The potential consequence of using longer windows is the dominance of stronger noise events at the expense of weaker events that are included in the same time window. Thus, virtual shot gathers obtained from longer time windows might not allow contribution from weaker noise sources originating from a variety of locations. In the case of the Aquistore site, the CO_2 reservoir is at a depth of approximately 3200 m or roughly 2 s two-way traveltime (Roach et al., 2015; White et al., 2015). Almagro Vidal et al. (2014) suggest that 10 s noise panels have optimum length to retrieve body-wave reflections down to a two-way traveltime of 2 s in a sedimentary

Table 1. Geometric properties of passive survey lines in the Aquistore site.

	L1 (west–east extension)		L2 (southwest extension)	
	June 2014	February 2015	June 2014	February 2015
Length (m)	~2302	~2302	~2447	~2447
No. of receivers	16[3]	27[4]	30[3]	26[4]
Receiver spacing (m)	~145	~72	~72	~72[5]
Geophone frequency (Hz)	10	10	10	10
Sampling rate (ms)	2	2	2	2
Receiver depth under surface (m)	20	20	20	20

[3]vertical component receivers
[4]vertical and 3C receivers
[5]Receiver spacing in some places is approximately 145 m.

basin. This window length ensures that noise panels would contain several free-surface multiples of the target reflections that help increase the signal-to-noise ratio in virtual shot gathers. Based on this, 10 s and one-hour noise panels were chosen for comparison.

To test the effects of time-window length for the data from the Aquistore site, we conducted two experiments. In the first experiment, seismic interferometry was performed on all one-hour noise panels for 23 days in June 2014 and for 13 days in February 2015. In the second experiment, we used 10 s noise panels for interferometric processing of two days of recorded noise from June 2014 and February 2015.

Visual inspection of noise panels prior to the retrieval of virtual shot gathers (Figure 2a–2d) shows some high-amplitude hyperbolic and linear events along L1 and L2, the geometry of which is consistent with reflected body waves originating from horizontal or steeply dipping geologic contacts. These could also be surface waves propagating in a direction perpendicular to the line (Figure 2a–2d). The energy of the noise panels is concentrated in the frequency range of 2–35 Hz (Figure 2e–2h). To better understand the time-variant nature of the noise energy at a receiver location, the power spectral density is calculated at the intersection of L1 and L2 (see the red star in Figure 1b and 1c). This is done for each hour-long noise panel from June 2014 and February 2015. Figure 2i shows the power spectral density for two weeks of noise from February 2015. Dominant power peaks are observed at approximately 7 and 13 Hz. The power spectral density characteristics of the noise from June 2014 are not shown here because they are similar.

To evaluate the temporal changes in the noise strength along L1 and L2, the root-mean-square (rms) amplitude is calculated for two days from the June 2014 and February 2015 data sets. Figure 3 shows amplitude graphs for these two days, which are also candidate days for the detailed study based on 10 s panels. We observe from the figure that, in general, the ambient noise from June 2014 is lower in amplitude than the noise from February 2015. In June 2014, both survey lines show amplitudes lower than 0.1 for the entire two days (Figure 3a–3d) except for a few very short intervals during which high-amplitude spikes are observed (for example, at hours two and four in Figure 3a–3d). In February 2015, the average amplitudes of the noise along L1 during days 1 and 2 are approximately 0.2 and 0.5, respectively (Figure 3e–3f). A few high-amplitude spikes are observed along L1 (for example at hour 11 on day 1 and hour 13 on day 2 in Figure 3e–3f). L2 data show consistent amplitudes of approximately 0.3 during days 1 and 2 (Figure 3g–3h). Some higher amplitude noise is present between hours 8 and 15 of day 1 (Figure 3g) and also at hours 13 and 14 of day 2 (Figure 3h).

To evaluate the directionality of the ambient noise sources at the Aquistore site, a beam-forming analysis was performed for L1 and L2 for noise recorded during June 2014 and February 2015. We used the algorithm applied by Cheraghi et al. (2015). A frequency range of 3–10 Hz was analyzed for velocities in the range of 1–5 km/s. The results from February 2015 are shown in Figure 4. The beam-forming results show the dominant propagation of waves from azimuths between 240° and 330° consistent with noise sources located near the Boundary Dam power plant, which is located approximately 3 km away at a bearing of 280° (Figure 1). Observed apparent velocities range from approximately 1.7 to 4.9 km/s with the strongest amplitude peaks occurring for velocities of 3–4 km/s. By comparison, the active-source 3D seismic data (Roach et al., 2015; White et al., 2015) exhibit direct body waves with a velocity of approximately 2500 m/s and surface waves with a velocity of approximately 500 m/s. Thus, the high-amplitude zones in Figure 4 with apparent velocities exceeding 2500 m/s are potentially associated with direct body waves, refracted P-waves, or P-wave reflections. The beam-forming results for June 2014 are also similar to those of February 2015 and are not shown here. Note that if refractions are present in the noise panels, application of seismic interferometry will retrieve virtual refrac-

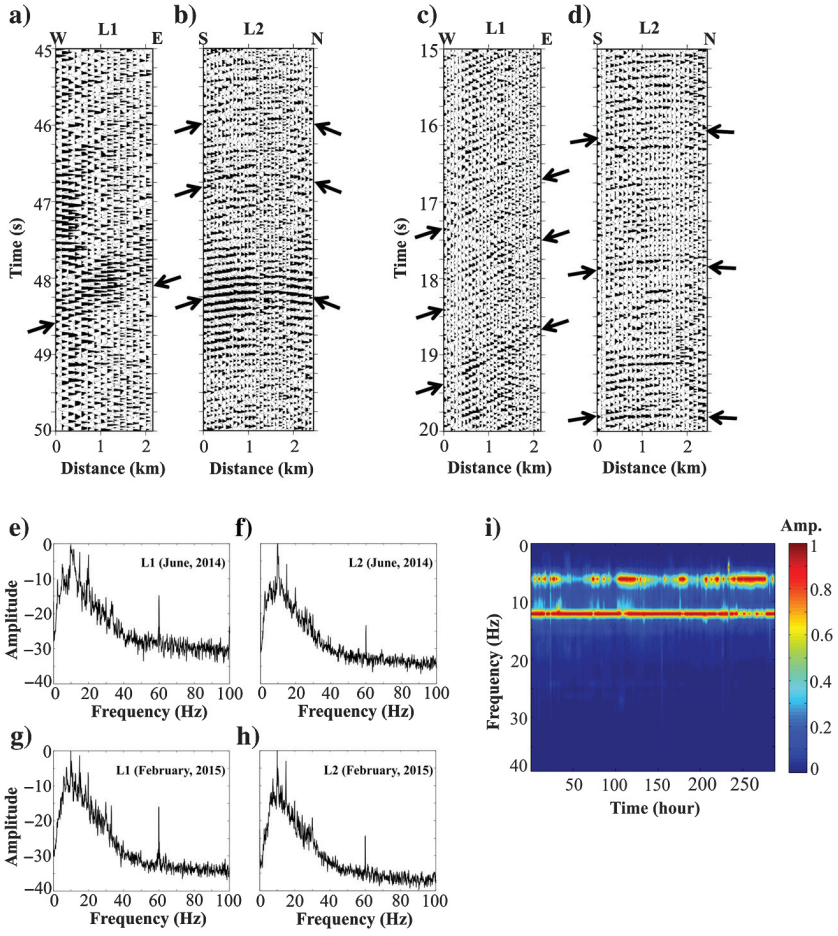

Figure 2. (a-b) Recorded noise along L1 and L2 (see Figure 1 for the location of the lines) from noise recorded in June 2014. (c-d) Recorded noise along L1 and L2 in February 2015. Arrows in panels (a-d) show steeply dipping and hyperbolic events corresponding to potential body waves. (e-h) Frequency spectra of recorded noise shown in panels (a-d), respectively. (i) Power spectral density graph for the receiver located at the cross point of L1 and L2 (see the red star in Figure 1) calculated for two weeks of recorded noise in February 2015. Two zones of high power density are observed at frequencies of 7 and 13 Hz. Amplitudes are normalized.

tions (Mikesell et al., 2009; Nichols et al., 2010), which might be quite prominent.

The observed anthropogenic seismic noise is primarily due to surface sources and appears to dominate the ambient noise in the area. Note that this is not obvious from the beam-forming analysis because we limited the velocity range to start from 1 km/s. The noise sources located close to or at the surface generate surface waves and body waves recorded by the passive lines. The body waves comprise direct waves, refracted waves, and they might also include reflected body waves with small angles to the horizontal (Figure 4). The former two body-wave arrivals will not contribute to retrieval of reflections in the application of seismic interferometry, whereas the latter will contribute to retrieval of reflections only at far offsets. This poses a significant challenge because crosscorrelation (equation 1) would retrieve surface and body waves whereas the CO_2 reservoir located at 3200 m depth requires illumination with body waves to be properly imaged.

Illumination diagnosis

Illumination diagnosis is applied to two days of passive data from the Aquistore site in June 2014 and in February 2015. We chose the receiver located at the intersection of L1 and L2 (Figure 1) for the virtual source position at which the illumination diagnosis is applied. We considered velocities between 500 and 2500 m/s as the limits for potential surface waves and velocities higher than 2500 m/s as velocities of potential body waves. This choice is based on a velocity of approximately 2500 m/s for first arrivals as determined from active-source shot gathers at the Aquistore site (Roach et al., 2015; White et al., 2015). Equation 3 is applied to all 10 s panels along L1 and L2 for the June 2014 and February 2015 data, where $\mathbf{x}_A$ is the receiver located at the intersection of both lines (Figure 1) and $\mathbf{x}_B$ represents the location of all other receivers along L1 and L2. Illumination diagnosis was applied in the crossline and inline directions of the 3D active-source seismic survey (Roach et al., 2015), which correspond to the L1 and L2

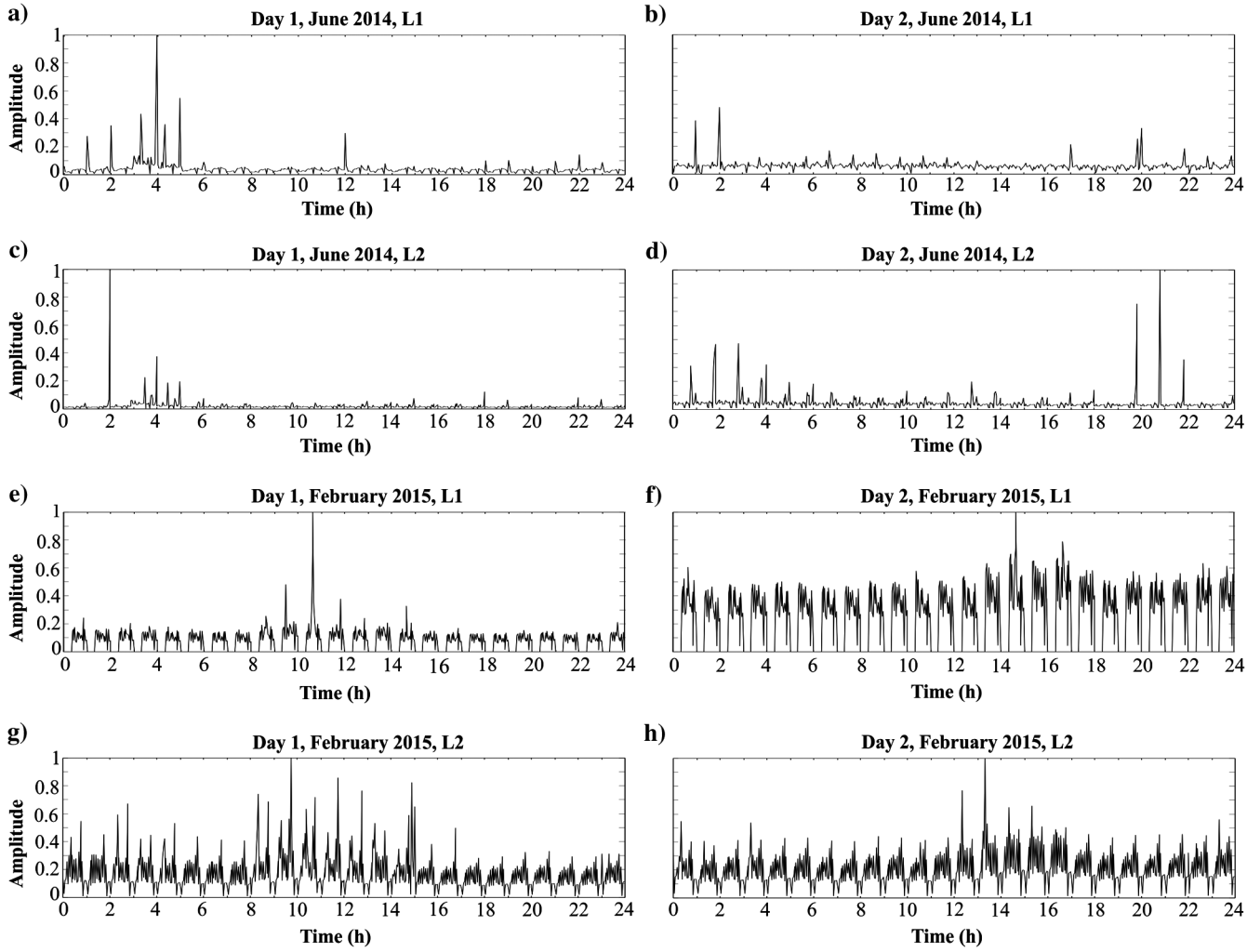

Figure 3. The rms amplitude calculated for two days of noise recorded in June 2014 along (a and b) L1 and (c and d) L2, respectively; rms amplitude calculated for two days of noise recorded in February 2015 along (e and f) L1 and (g and h) L2, respectively. In these graphs, for each hour, the 1 h rms amplitude for each individual array station is plotted; i.e., in essence, the graph comprises 24 subgraphs. The time along the horizontal axis is in Universal Time. The locations of L1 and L2 are shown in Figure 1. The rms amplitude is calculated in the frequency domain at each receiver location. In each graph shown in panels (a-h), the amplitudes are normalized to the maximum amplitude for the respective graph. The notches observed in panels (e-h) correspond to individual stations where data were not successfully recorded.

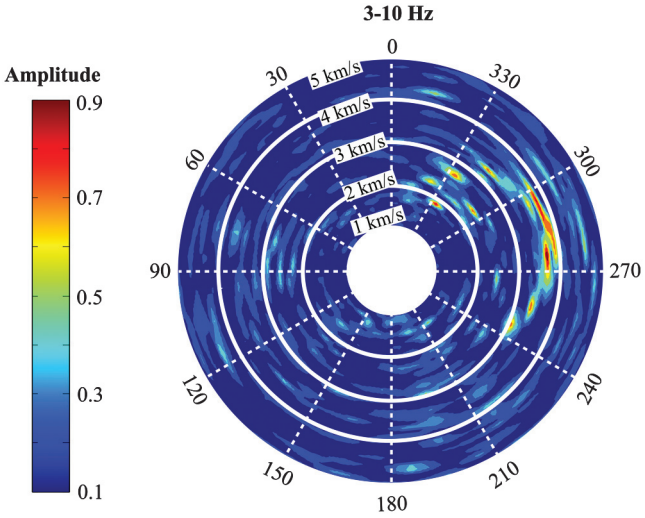

Figure. 4. Directional beam-forming analysis for recorded noise from February 2015 where the maximum beam power of each hourly panel and its apparent velocity and azimuth are shown for the frequency range of 3–10 Hz. The north direction has an azimuth of 0°. The azimuth increases to the west (i.e., counterclockwise).

orientations, respectively. Separate analyses were conducted for the June 2014 and February 2015 data. A total of 17,280 10 s noise panels are available for the two days of recording during both periods. The illumination diagnosis procedure took into account the varying number of receivers between both surveys.

Figure 5 shows the illumination diagnosis results from the intersection of L1 and L2 for one hour of noise recorded along L1 and L2 (Figure 1) during June 2014 and February 2015. Figure 5a and 5b shows the results for the noise recorded for hour 15 during day 2 of June 2014 (as an example). A total of 54 panels along L1 (Figure 5a, also see Table 2) and 35 panels along L2 (Figure 5b, also see Table 2) show dominant ray parameters (indicated with a black cross) corresponding to a velocity higher than 2500 m/s (slowness of ±0.0004 s/m). These are considered to be candidates of correlated noise panels that are dominated by body-wave noise. The remainder of the correlated noise panels is considered to be dominated by surface-wave noise (Figure 5a and 5b). Figure 5c and 5d shows the illumination diagnosis results of the recorded noise for hour one during day one of February 2015. Only 10 panels along L1 (Figure 5c, also see Table 3) and 85 panels along L2 have dominant ray parameters consistent with possible body-wave propagation. The correlated noise panels dominated by surface-wave noise from June 2014 (indicated by blue crosses in Figure 5a and 5b) do not

Figure 5. (a-b) Illumination-diagnosis results along L1 and L2 from recorded noise at hour 15 during day two in June 2014 (Table 2). (c-d) Illumination diagnosis results along L1 and L2 at hour one during day one in February 2015 (Table 3). Limits 1 and 2 show the calculated slowness for velocity of ±2500 m/s (slowness of ±0.0004 s/m). The black crosses within the limits identify noise panels likely dominated by body waves, i.e., an absolute value of velocity greater than 2500 m/s. Blue crosses outside that area are demonstrating noise panels dominated with surface waves, i.e., an absolute value of velocity between 500 to 2500 m/s.

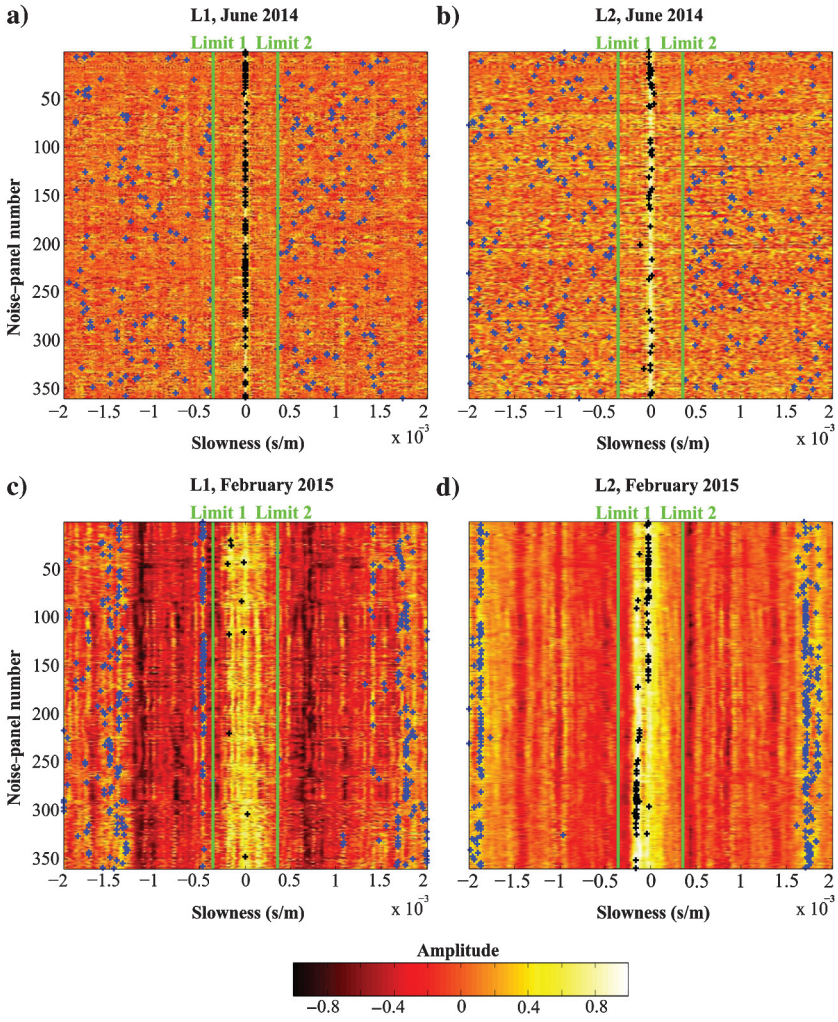

show any consistent velocity trends. In contrast, the surface-wave-dominated correlated noise panels for February 2015 exhibit propagation with specific apparent velocities. For example, in Figure 5c, slowness trends are observed at 0.0017 (~588 m/s), −0.0015 (~ − 666 m/s), and −0.0005 s/m (− ~ 2000 m/s). Figure 5d also shows two specific trends at approximately −0.0019 (~526 m/s) and 0.0017 s/m (~588 m/s). These clear patterns suggest a connection to a repeatable natural or anthropogenic source of the noise.

Virtual shot gathers were formed by summing only noise panels that were identified in the illumination diagnosis as body-wave-dominated panels along both the orthogonal lines (L1 and L2). With this definition, only 10 panels at hour 15 during day day in June 2014 (see Table 2 and also Figure 5a and 5b) and four panels at hour one during day one in February 2015 (see Table 3 and also Figure 5c–5d) qualify.

Tables 2 and 3 summarize the illumination diagnosis results for June 2014 and February 2015, respectively. During day one of June 2014, 19% and 16% of the correlated panels along L1 and L2, respectively, showed a dominant apparent velocity greater than 2500 m/s at the intersection of both lines (Figure 1). Of these panels, only 11% qualified simultaneously along both lines. During day two of June 2014, only 3% of the correlated noise panels qualified as body-wave-dominated simultaneously along both lines even though the proportions for L1 and L2 (13% and 10%) were comparable to day one.

Table 3 presents the results from the illumination diagnosis method for the two days of noise from February 2015. In general, the recorded noise along L1 in February 2015 shows fewer body-wave-dominated correlation panels than in June 2014 — only 2.6% for day one and 1.8% for day two along L1. In contrast, for L2, a high proportion of correlated noise panels qualify with 50%–51% for the two days. But, only 1.3%–1.7% qualifies simultaneously along both lines.

Virtual shot gathers

Virtual shot gathers were generated using equation 1. Precorrelation processing applied to the data was based on that described by Draganov et al. (2013) and Cheraghi et al. (2015). It included band-pass filtering (2–35 Hz) and trace-to-trace amplitude balancing (energy normalization). The chosen frequency range was based on the frequency spectra of the noise panels and the beam-forming analysis (Figures 2 and 4). Trace-by-trace amplitude balancing was applied to ensure that signals from all noise panels were equally weighted. Crosscorrelation is calculated between each possible pair of receiver locations along L1 and L2. For one panel, the crosscorrelation of noise for a specific receiver with noise from other receivers forms a virtual shot gather as if a shot was acquired at that specific receiver location. Crosscorrelations are calculated for each receiver pair along L1 and L2 (Figure 1), and then causal and acausal parts of the correlation results are summed to generate a correlated noise panel. Summing the causal and acausal crosscorrelation results takes into account the fact that some part of Green's function might be retrieved at positive times and other parts at negative times (Draganov et al., 2013; Cheraghi et al., 2015). Finally, all crosscorrelated noise panels are summed together to produce the final virtual shot gather for that specific virtual shot location.

Virtual shot gathers were generated using two different strategies. First, long (1 h) noise panels were used to produce virtual shot gathers. In total, 23 days of recorded noise from June 2014 and 13 days of noise from February 2015 were used resulting in 552 and 312 noise panels, respectively. In a second attempt designed to enhance energy from weaker sources, shorter (10 s) noise panels for two-day periods in June 2014 and February 2015 were used. These 10 s noise panels (17,280 panels for each two-day period) were then sub-

Table 2. Applying illumination diagnoses to recorded noise along L1 and L2 during two days in June 2014. Each hour contains 360 panels. Common panels refer to those panels along L1 and L2, which are dominated with body waves, simultaneously.

	June 2014, day 1			June 2014, day 2		
	body-wave panel/hour			body-wave panel/hour		
	L1	L2	Common panels	L1	L2	Common panels
Hour 1	17	11	-	118	97	65
Hour 2	21	9	6	29	4	3
Hour 3	149	111	95	16	6	2
Hour 4	298	261	247	35	17	2
Hour 5	282	251	232	70	55	29
Hour 6	63	37	22	88	46	29
Hour 7	4	6	2	49	30	9
Hour 8	6	6	2	32	24	7
Hour 9	32	44	17	19	16	2
Hour 10	88	84	64	37	52	9
Hour 11	50	48	30	20	25	3
Hour 12	31	39	17	34	21	4
Hour 13	24	23	15	46	10	2
Hour 14	33	21	13	56	21	8
Hour 15	51	19	16	54	35	10
Hour 16	18	8	1	53	40	13
Hour 17	22	12	1	61	46	13
Hour 18	19	18	1	59	54	15
Hour 19	65	46	21	49	63	16
Hour 20	37	25	4	39	28	6
Hour 21	35	28	4	44	43	13
Hour 22	105	80	50	64	45	16
Hour 23	126	102	55	45	72	15
Hour 24	117	96	58	24	31	2
Sum	1693	1385	973	1141	881	293

jected to illumination diagnosis in an attempt to reduce the effects of surface-wave noise. This winnowing resulted in a total of 1266 panels (Table 2) for June 2014 and 258 panels (Table 3) for February 2015.

Figure 6 displays examples of processed virtual shot gathers (see Table 4 for details of processing steps). The virtual shots are located at the intersection of L1 and L2 (Figure 1) and are generated from 1 h or 10 s noise panels for both time periods (June 2014 and February 2015). Direct P-wave arrivals (2500 m/s) and surface-wave arrivals (500 m/s) are observed on all virtual shots of L1. Note that the surface-wave arrivals are less prominent in the case in which body-wave illumination discrimination has been applied (Figure 6f and 6j), but they are nevertheless still visible, especially for receivers to the left of the virtual shot position. This again suggests that the dominant surface-wave noise source is to the right of the virtual shot location, i.e., the power plant. The fact that surface-wave arrivals are retrieved even after illumination discrimination suggests that the surface-wave removal based on illumination analysis as applied is ineffective. This means that the surface waves were continuously present in the recorded noise and that their amplitudes were comparable with the amplitudes of the body waves. Surface-wave arrivals are apparently not as strong on the virtual shot gathers of L2, but direct P-wave arrivals are not as obvious either (Figure 6). The subhorizontal events in the virtual shot gather for February 2015 (Figure 6d, 6k, and 6l) potentially could include reflections, but they might also include surface waves arriving from the northeast. The limited amount of predicted moveout across the geophone spread precludes definitive identification. On the other hand, the illumination diagnosis helps us here. As the illumination discrimination allows the summation of correlated noise panels that are characterized by dominant body-wave noise along both lines, it will suppress retrieval of surface-wave arrivals along L2 that arrive from the northeast. Because the virtual shot gathers in Figure 6g and 6k exhibit subhorizontal arrivals that are not present after illumination discrimination (Figure 6h and 6l, respectively), we conclude that such suppressed subhorizontal events are actually surface waves that arrived from the northeast. However, there are a few subhorizontal events that appear stronger after illumination discrimination (Figure 6l), suggesting that they are most probably body-wave arrivals.

Table 3. Applying illumination diagnoses to recorded noise along L1 and L2 during two days in February 2015. Each hour contains 360 panels. Common panels refer to those panels along L1 and L2, which are dominated with body waves, simultaneously.

	February 2015, day 1			February 2015, day 2		
	body-wave panel/hour			body-wave panel/hour		
	L1	L2	Common panels	L1	L2	Common panels
Hour 1	10	85	4	4	198	4
Hour 2	15	90	6	1	163	1
Hour 3	19	176	15	9	258	7
Hour 4	11	153	9	5	235	5
Hour 5	4	129	2	19	233	18
Hour 6	11	167	9	4	206	3
Hour 7	8	175	4	2	217	2
Hour 8	18	129	7	1	199	1
Hour 9	1	141	1	11	242	8
Hour 10	21	110	12	4	254	3
Hour 11	8	117	5	4	225	3
Hour 12	9	166	4	4	169	3
Hour 13	5	175	4	2	84	2
Hour 14	14	203	7	9	79	4
Hour 15	2	267	2	6	68	4
Hour 16	2	259	1	4	59	2
Hour 17	14	272	10	12	124	8
Hour 18	7	204	5	14	161	7
Hour 19	3	202	3	6	173	3
Hour 20	5	239	3	5	199	2
Hour 21	3	280	3	10	230	5
Hour 22	17	202	14	4	224	2
Hour 23	3	257	3	6	175	4
Hour 24	17	204	14	10	267	10
Sum	227	4402	147	156	4442	111

Virtual shots from L1 shown in Figure 6 are transformed to the f-k domain to investigate the ambient-noise signature. The f-k transformed images (Figure 7) indicate that most of the seismic signal has frequencies between 5 and 20 Hz except in Figure 7b (13 days of noise from February 2015), in which the signal is between 5 and 15 Hz. Aliased surface waves are also observed (the dashed areas in Figure 7). Their presence is another reason for the ineffectiveness of the illumination-diagnosis method because the method is not designed to eliminate aliased surface waves. Surface waves are less prominent in Figure 7e and 7f (corresponding to virtual shots shown in Figure 6i and 6j) probably due to the additional receivers used in February 2015 that provided better spatial sampling along L1. An example of a raw and processed virtual shot gather located at the intersection of L1 and L2 is shown in Figure 8 to demonstrate the effectiveness of the processing sequence (Table 4).

Passive seismic modeling

Synthetic passive seismic data were generated to assess the effects of the strong directionality of ambient noise at the Aquistore site and to provide a basis for comparison with the field data. The subsurface geology and seismic reflectivity at the Aquistore site is well-known based on the geophysical and geologic borehole logs and 3D active-source seismic surveys (Roach et al., 2015; White et al., 2015). For the passive seismic modeling, we constructed a simple 2D model consist-

ing of isotropic, laterally homogeneous layers based on the P-wave, S-wave, and density logs from the site (Figure 9). The P-wave velocities range from 2.5 to 6.3 km/s, whereas the S-wave velocities and densities (not shown) vary from 1 to 3 km/s, and 2 to 2750kg/m^3, respectively. The reservoir is located at depths greater than 3100 m.

A 2D finite-difference elastic algorithm (Thorbecke and Draganov, 2011) was used to simulate the passive seismic data along L1. Beam-forming analysis (Figure 4) showed that the ambient noise mostly propagates subparallel to the orientation of L1 and broadside to L2. For the modeling, source and receiver locations were chosen to be similar to the field acquisition geometries. For the L1 model, 30 receivers were placed at a depth of 20 m below the surface and distributed evenly along a distance of 2.5 km (receivers are distributed every 72 m between the arrows in Figure 9a). Random noise sources were located at shallow depths (less than 100 m) at distances of 1–2 km away from the receivers (i.e., within the dashed rectangle in Figure 9a). A maximum frequency of 35 Hz was used. A total of 360 noise panels, each 10 s long (for a total of one hour), were simulated and then summed to build one hour of noise data per receiver location. Synthetic virtual shots were retrieved by crosscorrelation (equation 1) using 10 s and 1 h noise panels. The synthetic virtual shot gathers were then subjected to a simplified CMP processing flow including (1) set-up geometry, (2) surface-wave removal (with application of median filter at velocities of 1.5–2 km/s), and (3) normal moveout (NMO) correction and stacking. The resultant synthetic stacked sections are shown in Figure 9b

Table 4. Processing steps applied to the retrieved shot gathers of the Aquistore site in June 2014 and February 2015.

1	Elevation corrections and set up geometry (the elevation datum is 600 m).
2	Picking theoretical line of first arrivals based on the coordinates of virtual shots and receivers and considering velocity of 2.5 km/s.
3	Top mute: 20 ms after the theoretical line of first arrivals.
4	Apply a median filter to remove potential surface and shear waves (at velocities of 1.5 & 2 km/s).
5	Apply a notch filter to remove coherent noise at frequencies 7 and 13 Hz.
6	Sorting to the CMP domain.
7	Amplitude balancing.
8	Velocity analysis in 2–5 km/s range (iterative).
9	NMO correction.
10	Stack.
11	Frequency-distance domain deconvolution.

Nominal fold of L1 in June 2014 and February 2015 is 9 and 14, respectively. Nominal fold of L2 in June 2014 and February 2015 is 14 and 13, respectively.

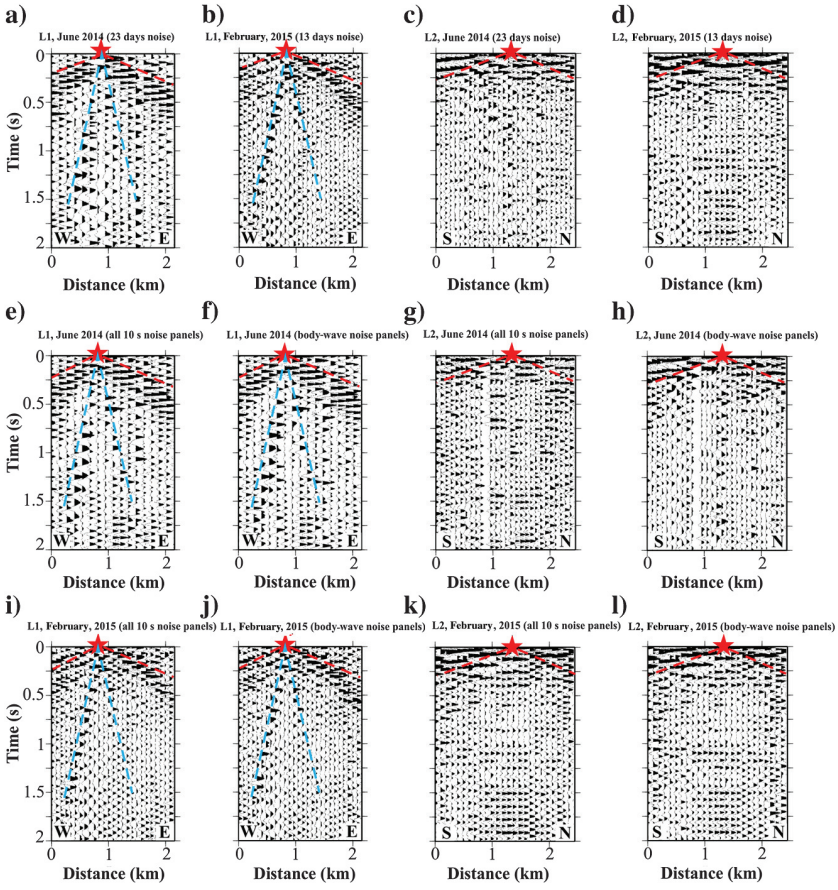

Figure 6. Virtual shot gather at intersections of L1 and L2 (Figure 1), (a) located on L1 and generated from 23 days recorded noise in June 2014, (b) located on L1 and generated from 13 days recorded noise in February 2015, (c) located on L2 and generated from 23 days recorded noise in June 2014, (d) located on L2 and generated from 13 days recorded noise in February 2015, (e) located on L1 and generated from all 10 s noise panels of two days recorded noise in June 2014, (f) located on L1 and generated from only body-wave noise panels of two days recorded noise in June 2014, (g) located on L2 and generated from all 10 s noise panels of two days recorded noise in June 2014, (h) located on L2 and generated from only body-wave noise panels of two days recorded noise in June 2014, (i) located on L1 and generated from all 10 s noise panels of two days recorded noise in February 2015, (j) located on L1 and generated from only body-wave noise panels of two days recorded noise in February 2015, (k) located on L2 and generated from all 10 s noise panels of two days recorded noise in February 2015, and (l) located on L2 and generated from only body-wave noise panels of two days recorded noise in February 2015. The red star shows the location of the cross point. The red dashed line presents the theoretical line of first arrivals, and the blue dashed line shows the surface-wave trajectory.

and 9c as obtained from 10 s and one-hour noise panels, respectively. A 1D P-wave velocity model extracted from the model shown in Figure 9a is shown in Figure 9d for comparison. In Figure 9, the interval from 0.8–1.6 s is well-imaged although the reflections fade toward the edges of the recording spread particularly at the west end of the line. This fading, however, is due to the acquisition geometry, i.e., due to the progressive lower stacking fold in the retrieved virtual CMP gathers. At greater depths, the reflectivity is weak, including at the reservoir (1.8–1.9 s). The NMO stacked sections generated with 10 s and 1 h noise panels are similar, although reflections from the reservoir zone have slightly higher amplitudes in the latter case.

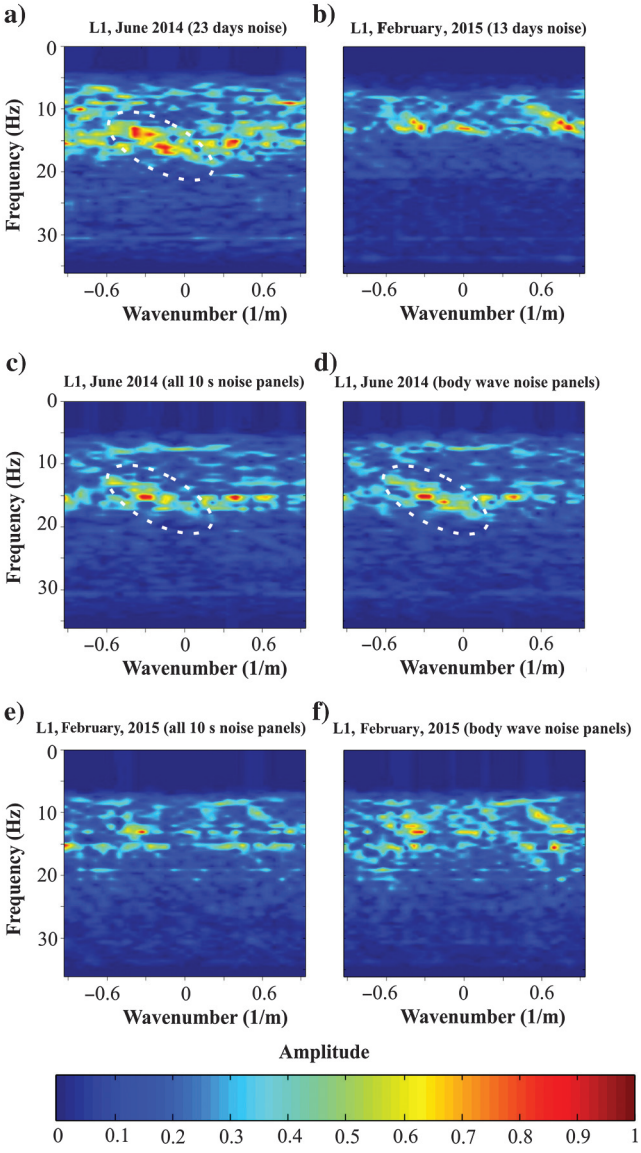

Figure 7. Shot gathers from Figure 6 transformed to the frequency-wavenumber (f-k) domain. (a) Located on L1 and generated from 23 days of recorded noise from June 2014, (b) located on L1 and generated from 13 days of recorded noise from February 2015, (c) located on L1 and generated from all 10 s noise panels for two days of recorded noise from June 2014, (d) located on L1 and generated from only body-wave noise panels for two days of recorded noise from June 2014, (e) located on L1 and generated from all 10 s noise panels for two days of recorded noise in February 2015, and (f) located on L1 and generated from only body-wave noise panels for two days of recorded noise from February 2015. The dashed area shows the aliased surface waves.

CMP imaging using virtual shot gathers

The virtual shot gathers generated from one-hour and 10 s noise panels from the Aquistore site were processed using a conventional seismic reflection CMP processing flow to evaluate the capability of passive seismic interferometry to image the main geologic formations at the Aquistore site. Table 4 shows the processing steps applied to the virtual shot gathers. The main processing steps include setting up geometry, picking of the theoretical line of first arrivals at a velocity of 2500 m/s (similar to the velocity of the first arrival in the active-source data), muting the virtual shot gathers above that line, applying a median filter to remove potential surface and shear waves at velocities of 1.5–2 km/s, applying a notch filter to remove coherent noise at frequencies of 7 and 13 Hz (Figure 2), velocity analysis, and stacking. The velocity model was chosen to have velocities similar to those applied for stacking of the active-source data.

Figures 10 and 11 show the resultant stack images for L1 and L2, respectively, for each of the two recording periods (June 2014 and February 2015) and for each noise panel summation strategy. Crossline and inline sections from the active-source seismic cube, corresponding to L1 and L2, are shown for comparison in each figure. The L1 sections for the June 2014 data (Figure 10b, 10c, and 10d) have some prominent subhorizontal reflections that extend continuously across the section as would be expected. Comparison with the active-source section indicates that the best correspondence occurs in the case in which all of the data from an extended period of noise recording (Figure 10b) are included. In this case, there is a good correspondence of reflections observed in the time interval of 0.5–1.5 s, whereas the ambient-noise images degrade at greater depths. Sections for the February 2015 data (Figure 10f, 10g, and 10h) are characterized by laterally discontinuous reflections and generally poor resemblance to the active-source section. This, though, is not surprising because the cumulative passive data in February 2015 is approximately 56% of that from June 2014. For both time periods, the sections with body-wave discrimination applied (Figure 10d and 10h) appear to partially improve the reflection image at the depth of the CO_2 storage reservoir along the western side (1.8–1.9 s). Recall that the level of ambient noise was higher during the February 2015 time period. All of the reflection images are compromised to some extent by strong dipping events that likely correspond to residual surface-wave and/or refracted-wave energy. Note that the illumination discrimination has improved the lateral continuity of the events (Figures 10d and 10h) compared with the events retrieved using all 10 s noise panels (Figure 10c and 10g).

The results for the north–south section (L2) are generally more variable (Figure 11). Whereas there appears to be an increase in overall reflectivity at approximately 0.75 s in some panels (Figure 11g and 11h) as observed in the active-source section, there is less correspondence between individual reflections as compared with L1. Note that the apparent reflectivity at approximately 0.75 s is increased in Figure 11g, but it is weaker in Figure 11h, which suggests that this might be an artifact due to surface waves propagating from the northeast. In contrast to L1, the more consistent results are

observed for the February 2015 recording period. The reflections in the June 2014 images along L2 are certainly less continuous laterally. Perhaps the best correlation is for the prominent reflection observed at approximately 1.15 s in the image for the February 2015 extended recording period (Figure 11f). A more detailed comparison is made from the best results of Figures 12 and 13 for L1 and L2. For L1 (Figure 12), correlation values for well-based synthetic seismograms over the window of 0.5–1.5 s are generally between 0.4 and 0.5 for static shifts of up to 50 ms. For comparison, much higher log correlation values (0.7–0.8) were obtained for the active-source section over this interval. For L1, the correlation value increases to 0.65 for a comparison window restricted to the interval in which the L1 image appears most robust (0.75–1.1 s). For L2 (Figure 13), the log correlation value is 0.5 for the 0.5–1.5 s window. The correlation value for L1 and L2 at their point of intersection is approximately 0.5 if a static shift of approximately 20 ms is applied.

As an alternative to CMP processing, autocorrelation for each receiver was conducted to directly generate zero-offset sections (Zhang et al., 2014; Boullenger et al., 2015) along L1 and L2. The quality of the resultant sections (not shown) was poor.

DISCUSSION

The ambient-noise images obtained in this study capture some of the primary reflectivity characteristics of the subsurface to depths of at least 1500 m. In particular, along L1 (Figure 11), reflections are prominent from the Lower Colorado shale (0.85 s, ~930 m), the Vanguard Formation (1.1 s, ~1100 m), and the Bakken shale (1.45–1.5 s, ~2100 m). In the case of L2 (Figure 13), a reflection from the Precambrian basement (1.9, ~3350 m) might be present. However, the ambient-noise images obtained for the limited duration of noise used do not achieve the fidelity that was originally anticipated based on the relatively simple geologic structure at the recording site and the consistent recording capability provided by a permanent buried array of geophones. The resultant reflection images show moderate correlation with colocated controlled-source reflection images that have been verified with well-log-based synthetic seismograms (Figures 12 and 13). The limited consistency of the ambient noise images achieved using 23 days of noise from 2014 and 13 days from 2015 makes the images of limited use for time-lapse analysis (Figures 10 and 11). This is likely due at least in part to using an inadequate length of recorded noise in the analysis for this site. Comparison of the results in Figure 10 (along the main direction

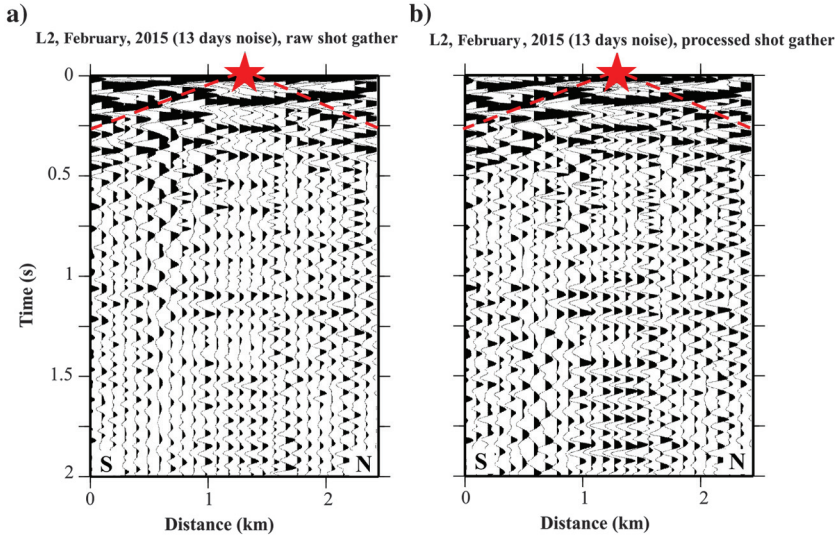

Figure 8. (a) Raw virtual shot gather from L2 located at the intersection of L1 and L2. (b) The same shot gather shown in panel (a) after application of the processing steps shown in Table 4; application of median and notch filtering, and also trace balancing. The virtual shot presented in panels (a and b) is for 13 days of recorded noise in February 2015. The virtual shot shown in panel (b) is the same virtual shot presented in Figure 6d.

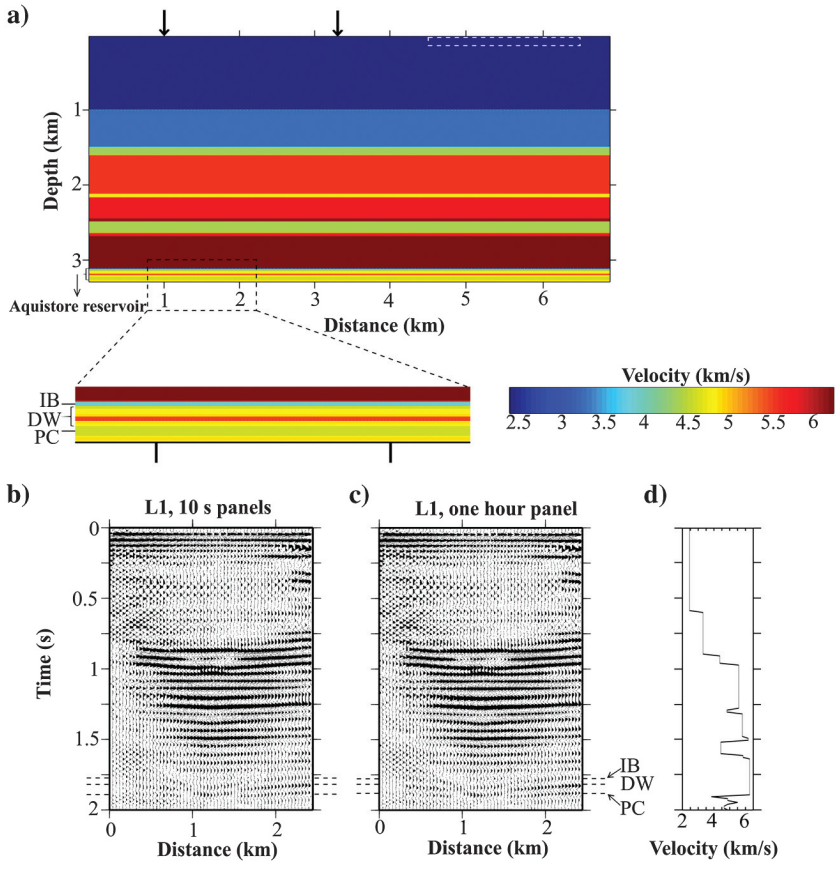

Figure 9. (a) P-wave velocity model for L1 based on borehole petrophysical measurements. Locations of random noise sources are restricted to the rectangular dashed area. An expanded view of the Aquistore reservoir is also shown in panel (a). (b-c) Synthetic stacked section along L1 generated from 10 s noise panels and one-hour noise panel, respectively. (d) The 1D velocity model extracted from the model shown in panel (a). Icebox shale (IB), Deadwood Formation (DW), and Precambrian rocks (PC) are geologic formations in the vicinity of the CO_2 reservoir.

of the noise) shows that using 23 days of noise results in a better image of the reflectors. This suggests that using a few months of noise may produce better results. The ambient-noise images (Figures 10 and 11) do not achieve the quality of images observed in the synthetic modeling exercise as shown in Figure 9. We believe that the largest contributing factors that degrade the ambient-noise imaging results are the unidirectional nature of the source noise, the generally low level of body-wave noise (relative to the dominant surface-wave noise) in this setting, and the time-variant nature of the ambient noise for this particular site.

Perhaps the dominant limiting factor in ambient-noise imaging at the Aquistore site is the directional nature of the noise. Ambient noise at the site emanates almost exclusively from near-surface sources at the nearby power plant site and from the nearby town of Estevan. This restricts the azimuth and the dip angle of the impinging noise wavefield at the recording site. This limitation affects the estimation of the Green's function and retrieval of body-wave reflections. Propagation of the ambient-noise wavefield only in a specific direction (see the beam-forming analysis in Figure 4) violates the assumptions underlying proper estimation of the Green's function (Wapenaar, 2004). This limiting imaging condition appears to be most severe along the imaging line (L2) that is orthogonal to the predominant direction of noise propagation (Figures 11 and 13). The effect of noise directivity also affected the application of the illumination diagnosis method because the apparent velocity of surface waves is dependent upon the orientation of the recording line. As a result, some surface-wave energy is likely misinterpreted as body-wave energy in the illumination diagnosis.

The synthetic modeling (Figure 9) that was conducted shows that good images should be achievable to intermediate depths (1–1.25 s) for profile L1 in spite of the unidirectional nature of the ambient-noise source. We have not modeled the case for L2, which is almost orthogonal to the main noise direction. The modeling results for L1 suggest that the source directionality is not the only limitation on imaging at the site. Another likely reason is the predominance of surface waves generated from the noise sources. This is supported

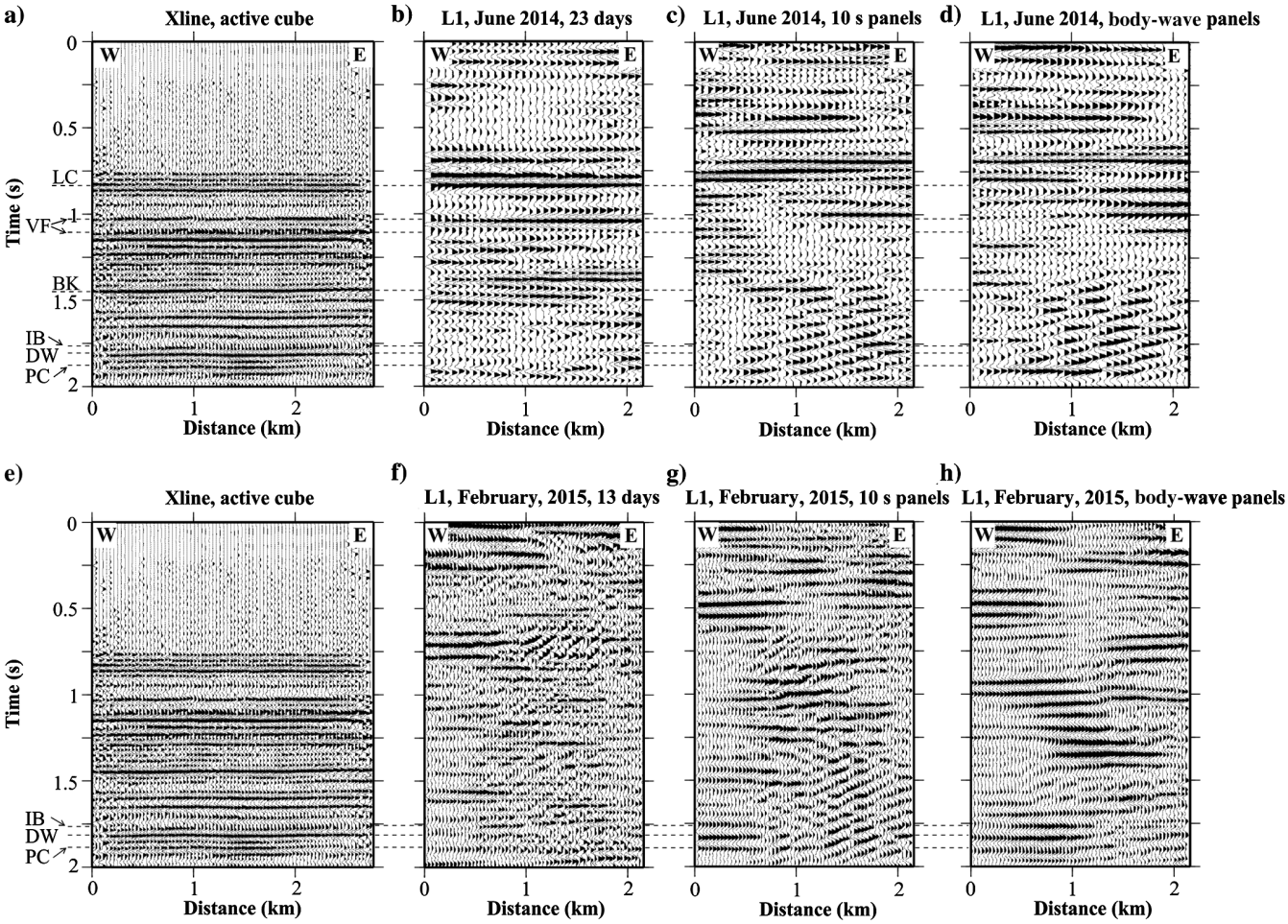

Figure 10. Comparison of (a) stacked image from a 3D active survey cube (from Roach et al., 2015) corresponding to the location of L1 (Figure 1) with L1 stacked images from (b) 23 days of recorded noise during June 2014, (c) all 10 s noise panels, and (d) potential body-wave noise panels of a two-day period in June 2014. (e) The same image shown in panel (a) for comparison with stacked image of L1 for (f) 13 days of recorded noise from February 2015, (g) all 10 s noise panels, (h) potential body-wave noise panels for two-day period in February 2015. Note that all images are filtered in 10, 12, 30, and 40 Hz, and the shape of the amplitude spectra was generally matched within the passband. The active-source images shown in panels (a and e) were generally devoid of frequencies lower than 10 Hz prior to filtering. LC, VF, and BK represent Lower Colorado shale, Vanguard Formation, and Bakken shale, respectively. IB, Icebox shale, DW, Deadwood Formation, and PC, Precambrian rocks are geologic formations in the vicinity of the CO_2 reservoir.

by the results from the illumination discrimination, which showed that for each of the analyzed days, only a small percentage of the 10 s noise panels were dominated by body-wave arrivals. Furthermore, even for the selected noise panels, the virtual shot gathers showed clear surface waves, meaning that the surface-wave noise was comparable in energy with the body-wave noise. This again suggests that due to the limited illumination, one might need to correlate longer noise recordings (may be 50 or 100 days) to obtain reliable images.

Comparison of the ambient-noise images obtained along either of the lines at recording times separated by eight months shows that they are significantly different (Figures 10 and 11). This is clear from the visual inspection. This is in spite of the noise direction remaining unchanged, receiver type, location, and coupling being kept constant and also in spite of using a consistent processing flow. It seems that some other factors may also be important such as variation of the noise power spectrum over time (Mehta et al., 2008) and variability in the noise amplitude between periods. Roach et al. (2015) show that high levels of repeatability (nrms values of 10%–20%) are required for time-lapse seismic monitoring of the Aquistore reservoir with expected CO_2-related changes in acoustic impedance in the range of −8 to −17%. This level of repeatability is clearly not achieved by the ambient noise images obtained in this study, but it might be improved by using longer duration noise recordings.

Image quality and suitability for time-lapse imaging require substantial improvement if this methodology is to be applicable for monitoring at the Aquistore site. It is clear that strategies must be used to overcome the unidirectional nature of the noise and its time-variant spectral characteristics. Noise directionality is likely the most difficult limitation to overcome because the power plant and related activities provide the primary source of noise. Other potential local noise sources that might improve the azimuthal coverage are limited to sparse vehicle traffic, road maintenance, well-site activities, and the operation of agricultural field equipment. All of these potential noise sources are sporadic or seasonal in nature, and thus, the selection of effective noise windows would be opportunistic. Additionally, the unidirectional nature of the ambient noise might be mitigated by using the full areal array of geophones (Figure 1) at the Aquistore site to allow 3D imaging.

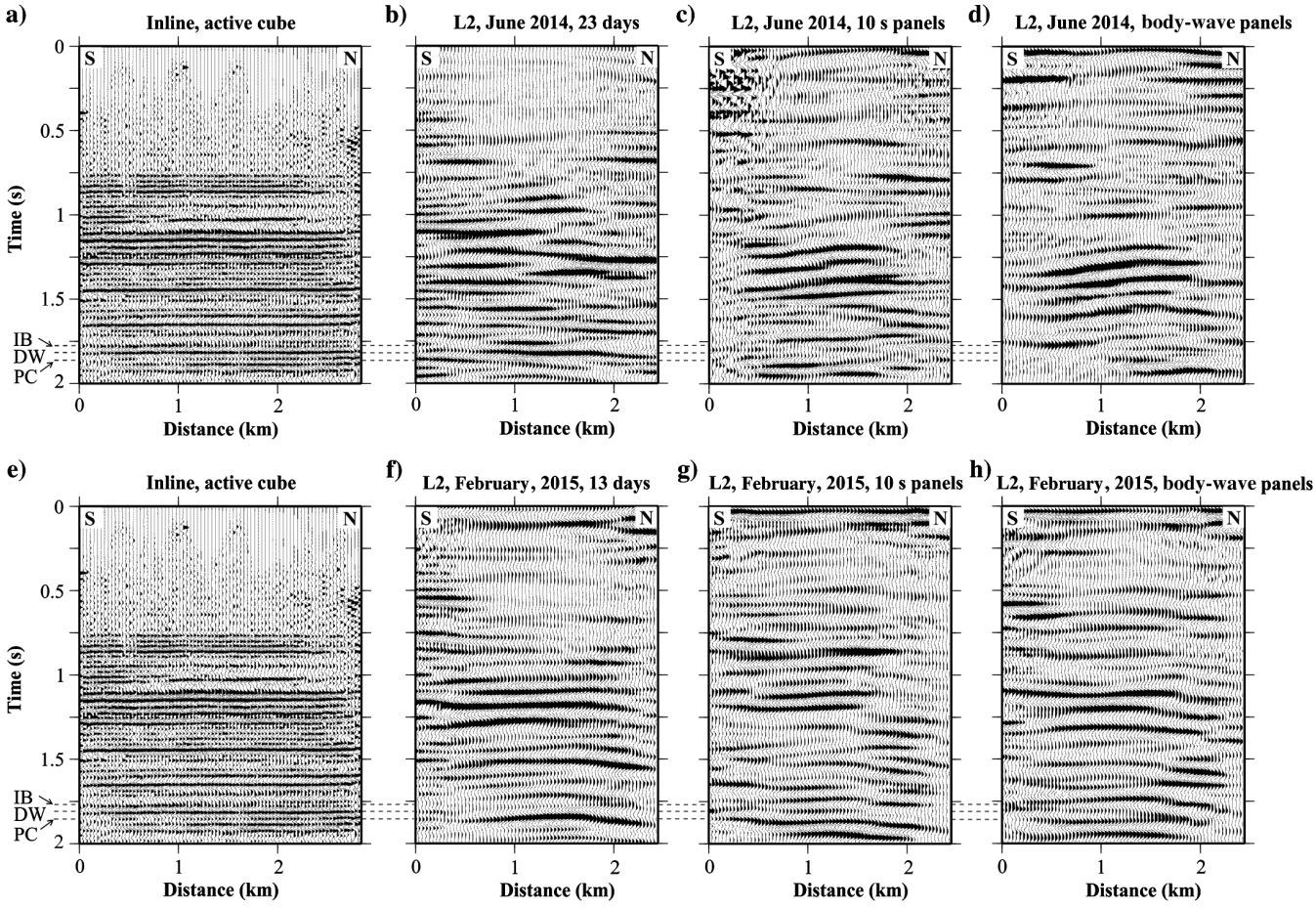

Figure 11. Comparison of (a) stack image from a 3D active survey cube (from Roach et al., 2015) corresponding to the location of L2 (Figure 1) with L2 stacked images from (b) 23 days of recorded noise from June 2014, (c) all 10 s noise panels, and (d) potential body-wave noise panels for a two-day period in June 2014. (e) The same image shown in panel (a) for comparison with stacked images of L2 for (f) 13 days of recorded noise in February 2015, (g) all 10 s noise panels, (h) potential body-wave noise panels of two-day period in February 2015. Note that all images are filtered in 10, 12, 30, and 40 Hz, and the shape of the amplitude spectra was generally matched within the passband. The active-source images shown in panels (a and e) were generally devoid of frequencies lower than 10 Hz prior to filtering. IB, Icebox shale, DW, Deadwood Formation, and PC, Precambrian rocks are geologic formations in the vicinity of the CO_2 reservoir.

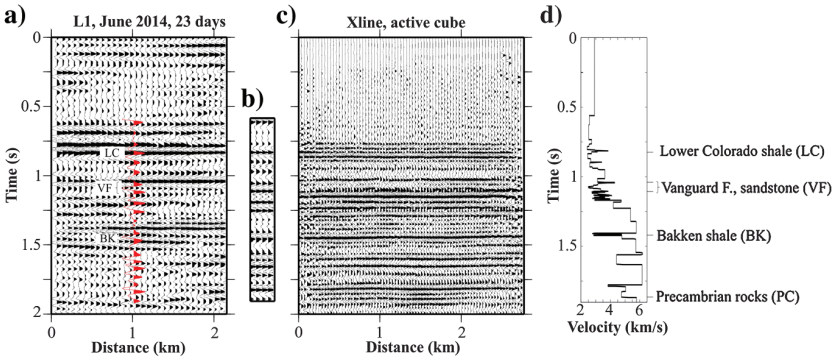

Figure 12. Comparison of a 1D log-based synthetic seismogram with an L1 stack image and a crossline image from the active-source cube, and panel (a) is the same image as shown in Figure 10b. (b) Synthetic seismogram generated from a wavelet extracted from the data shown in panel (a) convolved with borehole log-based reflectivity. The superposed wiggle trace in panel (a) is the same trace shown in panel (b). (c) The same image as shown in Figure 10a and 10e. (d) Depth-to-time converted P-wave velocity log. LC, VF, BK, and PC represent the Lower Colorado shale, Vanguard Formation, Bakken shale, and Precambrian, respectively. Note that images shown in panels (a and c) are filtered in 10, 12, 30, and 40 Hz. The active-source image shown in panel (c) does not contain frequencies lower than 10 Hz. This image was extracted from the 3D active-source cube acquired in 2012 (Roach et al., 2015).

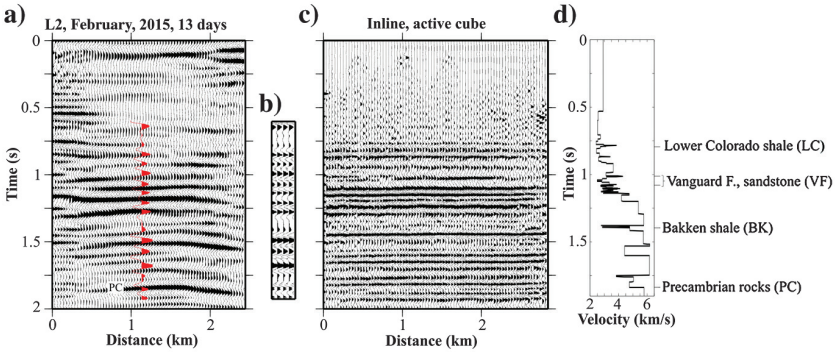

Figure 13. Comparison of a 1D log-based synthetic seismogram with an L2 stack image and an image from the inline direction of the active-source cube, panel (a) is the same image as shown in Figure 11f. (b) Synthetic seismogram generated from a wavelet extracted from the data shown in panel (a) convolved with borehole log-based reflectivity. The superposed wiggle trace in panel (a) is the same trace as shown in panel (b). (c) The same image as shown in Figure 11a and 11e. (d) Depth-to-time converted P-wave velocity log. LC, VF, BK, and PC represent Lower Colorado shale, Vanguard Formation, Bakken shale, and Precambrian, respectively. Note that images shown in panels (a and c) are filtered in 4, 5, 30, and 40 Hz. The active-source image shown in panel (c) does not contain frequencies lower than 10 Hz. This image was extracted from 3D active-source cube acquired in 2012 (Roach et al., 2015).

To address the temporal spectral variations in the ambient noise sources, a more deliberate selection of noise windows for processing from longer duration noise recordings is required in which the spectral characteristics are matched in some fashion. Clearly, this means that time-lapse monitor images may be restricted to certain times during the year.

CONCLUSIONS

We applied CMP reflection imaging to virtual shot gathers retrieved by seismic interferometry from ambient-noise data acquired along two orthogonal arrays of geophones at the Aquistore CO_2 storage site. The purpose of the study was to image the subsurface geology at the storage site and to assess the potential for time-lapse seismic imaging in the vicinity of the storage reservoir at 3200 m depth. This analysis has led to the following conclusions: (1) The resultant low-fold 2D seismic images bear a moderate resemblance to 2D sections from a high-fold active-source 3D seismic cube after the appropriate band-pass filtering has been applied. Moderate correlation values of approximately 0.5 are achieved for the ambient-noise images and well-based synthetic seismograms. (2) The quality of the ambient-noise images is limited by the unidirectional and very low body-to-surface-wave ratio of the local noise sources. Directional analysis indicates that the local power plant and nearby associated industrial activities are the main noise sources. (3) Illumination diagnosis applied to two days of ambient noise provided an insufficient number of body-wave-dominated noise panels to help improve the retrieval of reflection arrivals. (4) The best ambient-noise images were achieved when the duration of recorded noise was maximized (13 and 23 days versus two days). (5) The ambient-noise images obtained at recording times separated by eight months are significantly different, although there were no expected changes in the subsurface over this time period. Substantial improvements in the repeatability of the images will be required before this methodology can be used for time-lapse imaging at the Aquistore site. Possible improvements might be achieved by using longer noise recordings (may be 50 or 100 days), using the areal array of geophones for 3D imaging, and by strategic selection of time periods for analysis to better match the spectral characteristics of the predominant noise sources.

ACKNOWLEDGMENTS

The Aquistore CO_2 Storage Project is managed by the Petroleum Technology Research Centre, Regina, Canada. I. Marsden conducts the monthly maintenance of the Aquistore permanent array. GLOBE Claritas™ was used for the seismic data processing. The Generic Mapping Tools from P. Wessel and W. H. F. Smith were used to prepare some of the figures. We thank editor M. Sacchi and four anonymous reviewers for their constructive comments and suggestions. This is publication 20160347 of the Geological Survey of Canada.

REFERENCES

Almagro Vidal, C., D. Draganov, J. van der Neut, G. Drijkoningen, and K. Wapenaar, 2014, Retrieval of reflections from ambient noise using illumination diagnosis: Geophysical Journal International, **198**, 1572–1584, doi: 10.1093/gji/ggu164.

Arts, R. J., X. Zhang, A. R. Verdel, D. Santonico, J. A. C. Meekes, R. P. Noorlandt, B. F. Paap, and V. P. Vandeweijer, 2013, Experiences with a permanently installed seismic monitoring array at the CO_2 storage site at Ketzin (Germany) — A status overview: Energy Procedia, **37**, 4015–4023, doi: 10.1016/j.egypro.2013.06.301.

Behm, M., G. M. Leahy, and R. Snieder, 2014, Retrieval of local surface wave velocities from traffic noise — An example from the La Barge basin (Wyoming): Geophysical Prospecting, **62**, 223–243, doi: 10.1111/1365-2478.12080.

Boullenger, B., A. Verdel, B. Paap, J. Thorbecke, and D. Draganov, 2015, Studying CO_2 storage with ambient-noise seismic interferometry: A combined numerical feasibility study and field-data example for Ketzin, Germany: Geophysics, **80**, no. 1, Q1–Q13, doi: 10.1190/geo2014-0181.1.

Cheraghi, S., A. J. Craven, and G. Bellefleur, 2015, Feasibility of virtual source reflection seismology using interferometry for mineral exploration: A test study in the Lalor Lake VMS mining area, Manitoba, Canada: Geophysical Prospecting, **63**, 833–848, doi: 10.1111/1365-2478.12244.

Draganov, D., X. Campman, J. Thorbecke, and A. Verdel, 2013, Seismic exploration-scale velocities and structure from ambient seismic noise (>1Hz): Journal of Geophysical Research: Solid Earth, **118**, 1–16.

Draganov, D., X. Campman, J. Thorbecke, A. Verdel, and K. Wapenaar, 2009, Reflection imaging from ambient seismic noise: Geophysics, **74**, no. 5, A63–A67, doi: 10.1190/1.3193529.

Draganov, D., K. Wapenaar, W. Mulder, J. Singer, and A. Verdel, 2007, Retrieval of reflections from seismic background-noise measurements: Geophysical Research Letters, **34**, L04305, doi: 10.1029/2006GL028735.

Eiken, O., P. Ringrose, C. Hermanrud, B. Nazarian, T. A. Torp, and L. Høier, 2011, Lessons learned from 14 years of CCS operations: Sleipner, In Salah and Snøhvit: Energy Procedia, **4**, 5541–5548, doi: 10.1016/j.egypro.2011.02.541.

Gassenmeier, M., C. Sens-Schönfelder, M. Delatre, and M. Korn, 2015, Monitoring of environmental influences on seismic velocity at the geological storage site for CO_2 in Ketzin (Germany) with ambient seismic noise: Geophysical Journal International, **200**, 524–533, doi: 10.1093/gji/ggu413.

Ivandic, M., C. Yang, S. Lüth, C. Cosma, and C. Juhlin, 2012, Time-lapse analysis of sparse 3D seismic data from the CO_2 storage pilot site at Ketzin, Germany: Journal of Applied Geophysics, **84**, 14–28, doi: 10.1016/j.jappgeo.2012.05.010.

Jeong, S., and J. Byun, 2014, Effective suppression of spurious events when generating reflected P- and PS-waves data using seismic interferometry: Journal of Applied Geophysics, **106**, 14–22, doi: 10.1016/j.jappgeo.2014.04.002.

Mehta, K., J. L. Sheiman, R. Snieder, and R. Calvert, 2008, Strengthening the virtual source method for time-lapse monitoring: Geophysics, **73**, no. 3, S73–S80, doi: 10.1190/1.2894468.

Mikesell, T.D., K. van Wijk, A. Calvert, and M. Haney, 2009, The virtual refraction: useful spurious energy in seismic interferometry: Geophysics, **74**, no. 3, A13–A17, doi: 10.1190/1.3095659.

Nakata, N., R. Snieder, T. Tsuji, K. Larner, and T. Matsuoka, 2011, Shear wave imaging from traffic noise using seismic interferometry by cross-coherence: Geophysics, **76**, no. 6, SA97–SA106, doi: 10.1190/geo2010-0188.1.

Nichols, J., D. Mikesell, and K. van Wijk, 2010, Application of the virtual refraction to near-surface characterization at the boise hydrogeophysical research site: Geophysical Prospecting, **58**, 1011–1022.

Poli, P., H. A. Pedersen, and M. Campillo, and , the POLENET/LAPNET Working Group, 2012, Emergence of body waves from crosscorrelation of short period seismic noise: Geophysical Journal International, **188**, 549–558, doi: 10.1111/j.1365-246X.2011.05271.x.

Roach, L. A. N., D. J. White, and B. Roberts, 2015, Assessment of 4D seismic repeatability and CO_2 detection limits using a sparse permanent land array at the Aquistore CO_2 storage site: Geophysics, **80**, no. 2, WA1–WA13, doi: 10.1190/geo2014-0201.1.

Roux, P., K. G. Sabra, P. Gerstoft, and W. A. Kuperman, 2005, P-waves from cross-correlation of seismic noise: Geophysical Research Letters, **32**, L19303, doi: 10.1029/2005GL023803.

Ruigrok, E., X. Campman, D. Draganov, and K. Wapenaar, 2010, High-resolution lithospheric imaging with seismic interferometry: Geophysical Journal International, **183**, 339–357, doi: 10.1111/j.1365-246X.2010.04724.x.

Ruigrok, E., X. Campman, and K. Wapenaar, 2011, Extraction of P-wave reflections from microseisms: Comptes Rendus Geoscience, **343**, 512–525, doi: 10.1016/j.crte.2011.02.006.

Thorbecke, J. W., and D. Draganov, 2011, Finite-difference modeling experiments for seismic interferometry: Geophysics, **76**, no. 6, H1–H18, doi: 10.1190/geo2010-0039.1.

Wapenaar, K., 2004, Retrieving the elastodynamic Green's function of an arbitrary inhomogeneous medium by crosscorrelation: Physics Review Letter, **93**, 254301-1–254301-4, doi: 10.1103/PhysRevLett.93.254301.

White, D. J., 2013a, Seismic characterization and time-lapse imaging during seven years of CO_2 flood in the Weyburn Field, Saskatchewan, Canada: International Journal of Greenhouse Gas Control, **16S**, S78–S94, doi: 10.1016/j.ijggc.2013.02.006.

White, D. J., 2013b, Toward quantitative CO_2 storage estimates from time-lapse 3D seismic travel times: An example from the IEA GHG Weyburn–Midale CO_2 monitoring and storage Project: International Journal of Greenhouse Gas Control, **16S**, S95–S102, doi: 10.1016/j.ijggc.2013.01.047.

White, D. J., C. D. Hawkes, and B. J. Rostron, 2016, Geological characterization of the Aquistore CO_2 storage site from 3D seismic data: International Journal of Greenhouse Gas Control, **54**, 330–344, doi: 10.1016/j.ijggc.2016.10.001.

White, D. J., L. A. N. Roach, and B. Roberts, 2015, Time-lapse seismic performance of a sparse permanent array: Experience from the Aquistore CO_2 storage site: Geophysics, **80**, no. 2, WA35–WA48, doi: 10.1190/geo2014-0239.1.

Worth, K., D. J. White, R. Chalaturnyk, J. Sorensen, C. Hawkes, B. Rostron, J. Johnson, and A. Young, 2014, Aquistore Project measurement, monitoring and verification: From concept to CO_2 injection: 12th International Conference on Greenhouse Gas Control Technologies, GHGT-12: Energy Procedia, **63**, 3202–3208.

Xu, Z., C. Juhlin, O. Gudmundsson, F. Zhang, C. Yang, A. Kashubin, and S. Luth, 2012, Reconstruction of subsurface structure from ambient seismic noise: An example from Ketzin, Germany: Geophysical Journal International, **189**, 1085–1102, doi: 10.1111/j.1365-246X.2012.05411.x.

Zhang, J., P. Gerstoft, and P. M. Shearer, 2009, High-frequency P-wave seismic noise driven by ocean winds: Geophysical Research Letters, **36**, L09302.

Zhang, F., C. Juhlin, and D. Sopher, 2014, Passive seismic ambient noise correlation: An example from the Ketzin experimental CO_2 storage site, Germany: Energy Procedia, **59**, 90–96, doi: 10.10.1016/j.egypro.2014.10.353.